Journal of Geodesy (2021) 95:98
https://doi.org/10.1007/s00190-021-01556-y

ORIGINAL ARTICLE

An improved tropospheric mapping function modeling method for space geodetic techniques

Yaozong Zhou[1] · Yidong Lou[1,2] · Weixing Zhang[1] · Jingna Bai[1] · Zhenyi Zhang[1]

Received: 8 February 2021 / Accepted: 4 August 2021 / Published online: 14 August 2021

Abstract
The accuracy of the tropospheric mapping functions is greatly influenced by the mapping function modeling methods. In the past decades, the 'fast' method rather than the rigorous least-squares methods was dominantly used for the development of mapping functions, such as Vienna Mapping Functions 1 (VMF1), considering the convergence issue and computation efficiency. In this study, we reconsider the suitability of the rigorous least-squares methods in operational mapping function development and present a new mapping function modeling method where the number of to-be-estimated coefficients in the mapping function continued fraction is adaptively determined according to the convergence in the least-squares fitting. The modeling accuracy of the new method is evaluated during 40 days spanning four seasons in 2020 at globally distributed 905 Global Navigation Satellite Systems (GNSS) stations. Significant improvement of the new method to the 'fast' method is found, with hydrostatic and wet mapping function modeling mean absolute errors (MAEs) of 1.6 and 1.3 mm for the new method and of 3.6 and 3.0 mm for the 'fast' method, respectively. Multi-GNSS Precise Point Positioning (PPP) of the new method is conducted at 107 International GNSS Service (IGS) Multi-GNSS Experiment (MGEX) stations. Effectiveness of the new method is also found for the PPP station height and zenith total delay estimation.

Keywords Space geodetic technique · Tropospheric mapping function · Modeling method · Modeling accuracy · Multi-GNSS PPP

1 Introduction

The signals of space geodetic techniques, such as Very Long Baseline Interferometry (VLBI) and Global Navigation Satellite Systems (GNSS), travel through the neutral atmosphere and experience the tropospheric slant path delays (SPDs) (Böhm and Schuh 2004, 2007; Böhm et al. 2006; Liu et al. 2020) that are usually modeled as zenith path delay (ZPD), mapping function and horizontal gradient and need careful corrections in data processing (Böhm and Schuh 2007; Landskron and Böhm 2018a, b). The mapping function carries out the interconversion between the ZPDs and SPDs and is usually modeled in the continued fraction form as (Marini 1972; Herring 1992)

$$mf(e) = \frac{1 + \frac{a}{1+\frac{b}{1+c}}}{sin(e) + \frac{a}{sin(e)+\frac{b}{sin(e)+c}}} \quad (1)$$

where mf and e represent mapping factor and elevation angle and a, b and c stand for mapping function coefficients. The continued fraction is based on the assumption of spherically symmetry of the troposphere (Marini 1972) and therefore can work well on the spherical shell model of the refractivity variations (Niell 1996) or an exponential profile (Marini 1972). Based on the continued fraction as shown in Eq. (1), different mapping function modeling methods were designed to better handle the three mapping function coefficients.

The first method is the rigorous method that determines all three coefficients with iterative least-squares adjustment, which was called as Vienna Mapping Functions VMF(rig), Marini 3 or VMF_{LSM} in previous studies

✉ Yidong Lou
ydlou@whu.edu.cn

Weixing Zhang
zhangweixing89@whu.edu.cn

[1] GNSS Research Center, Wuhan University, Wuhan, P. R. China

[2] State Key Laboratory of Information Engineering in Surveying, Mapping and Remote Sensing, Wuhan University, Wuhan, P. R. China

(denoted as MFlsmabc hereafter), by fitting ray-traced mapping factors at several specific outgoing elevation angles (Niell 1996; Böhm and Schuh 2004; Urquhart et al. 2014; Lu et al. 2016; Landskron and Böhm 2018b). However, the MFlsmabc method cannot achieve convergence in the iteration process when the actual tropospheric state greatly departs from the spherically symmetric or exponential assumptions, which is more common for the wet coefficients (a_w, b_w and c_w), mainly caused by the complex variations of the atmospheric water vapor (Landskron and Böhm 2018b). This method is therefore generally applied in the determination of empirical coefficients from the monthly mean numerical weather model products which smooth the complex atmospheric water vapor variations (Landskron and Böhm 2018b). To avoid the convergence issue in the MFlsmabc method, the simplified method ($VMF3_{LSM}$) (referred as MFlsma hereafter) that only estimates the coefficient a by fixing the empirical b and c coefficients was proposed (Landskron and Böhm 2018b). Though the MFlsma method can completely avoid the convergence problem in the MFlsmabc method, the accuracy is somewhat degraded (Landskron and Böhm 2018b).

In addition to the least-squares methods, the most commonly used method is the 'fast' method, generally named as VMF(fast) or $VMF3_{3deg}$ in previous studies (referred as MFfast in this paper) (Böhm and Schuh 2004; Landskron and Böhm 2018b). Only one coefficient, a, is calculated from the mapping factor at 3° outgoing elevation angle or 3.3° initial elevation angle with fixing coefficients b and c as shown in Eq. 2 (Böhm and Schuh 2004; Landskron and Böhm 2018b). The MFfast method is simple and efficient, whereas its accuracy further decreases compared with the MFlsma method (Landskron and Böhm 2018b).

$$a = -\frac{mf(e) \bullet \sin(e) - 1}{\frac{mf(e)}{\sin(e)+\frac{b}{\sin(e)+c}} - \frac{1}{1+\frac{b}{1+c}}} \tag{2}$$

To date, the commonly used VMF1 (Böhm et al. 2006), University of New Brunswick (UNB) VMF1 (UNB-VMF1) (Santos et al. 2012) and German Research Center for Geosciences (GFZ) VMF1 (GFZ-VMF1) (Zus et al. 2015) adopt the MFfast method and the newly published VMF3 employs the MFlsma method (Landskron and Böhm 2018b). However, the more accurate MFlsmabc method is actually ignored in the operational mapping function modeling, without detailed investigations of the convergence and accuracy for the method in current studies.

In this study, on the basis of the existing MFlsmabc, MFlsma and MFfast methods, we will additionally introduce the least-squares method that estimates the coefficients a and b, with the empirical coefficient c fixed (referred as MFlsmab). A new method, referred as MFlsmcom, is then proposed, by combining the three least-squares methods (MFlsmabc, MFlsma and MFlsmab) and the MFfast method based on their convergences. The detailed descriptions of the five methods are in Sect. 2. In Sect. 3, we comprehensively evaluate the modeling cost time, convergence ratio and modeling residual error of the five methods. In Sect. 4, we validate the mapping functions from the fully convergent MFlsma, MFfast and MFlsmcom methods by the ray-traced tropospheric delay. In Sect. 5, we apply the mapping functions developed by using the MFlsma, MFfast and MFlsmcom methods, respectively, in multi-GNSS Precise Point Positioning (PPP) analyses (Zumberge et al. 1997) and compare the coordinate repeatability and the impacts on GNSS estimates. In Sect. 6, we summarize the mapping function modeling performance and multi-GNSS PPP performance of different methods.

2 Mapping function modeling methods

2.1 MFlsmabc method

The MFlsmabc method is the most rigorous and accurate method that estimates all three coefficients a, b and c with iterative least-squares adjustment (Landskron 2017; Landskron and Böhm 2018b). The ray-traced mapping factors at several specific outgoing elevation angles are taken as modeling inputs. The initial values of coefficients are taken from the Global Pressure and Temperature 3 (GPT3) model (for a) and spherical harmonics series (for b and c). If the coefficient increments between two consecutive iterations are smaller than 10^{-8}, the convergence is achieved. The numbers of iterations are limited to 5 and 10 for the hydrostatic and wet coefficients, respectively, for saving modeling cost time. We found that there exist unrealistic jumps in the mapping factor at specific elevation angle when part of the estimated coefficients is negative as shown in Fig. 1 for two examples. These situations are therefore taken as un-convergent in this study.

2.2 MFlsma method

The MFlsma method only estimates the mapping function coefficient a (Landskron 2017; Landskron and Böhm 2018b), with the initial value from the GPT3 model, and the b and c coefficients are fixed to the spheric harmonic values. If only one mapping factor at 3° outgoing elevation angle is used, the MFlsma method is equivalent to the MFfast method. The iterative conditions are same as the MFlsmabc method. Theoretically, the MFlsma method can always reach convergence if no limitation of the iterations is set.

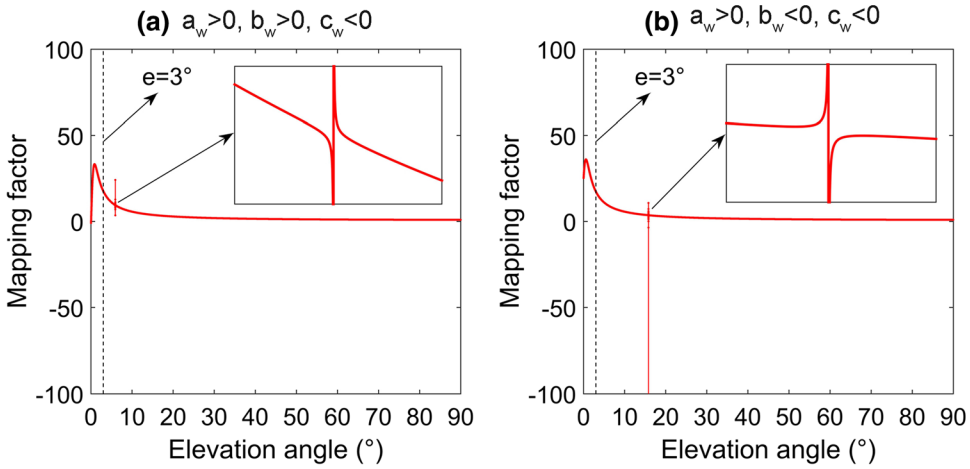

Fig. 1 Fitting curves of wet mapping function coefficients by the MFlsmabc method. The a_w, b_w and c_w values are 0.00021845, 0.00003936 and − 0.10361254 for the left case **a** and are 0.00032387, − 0.00211557 and − 0.26450967 for the right case **b**

2.3 MFfast method

The MFfast method is the most commonly used method that analytically calculates the coefficient a according to Eq. 2 with the mapping factor at 3° outgoing elevation angle or 3.3° initial elevation angle (Böhm and Schuh 2004; Landskron 2017; Landskron and Böhm 2018b) and fixes the empirical b and c coefficients to the spheric harmonic values. The method does not need the iterative calculation and is the most efficient method.

2.4 MFlsmab method

A compromised method, denoted as MFlsmab, that estimates a, b coefficients with the initial values of a and b coefficients from the GPT3 model and the spherical harmonics series, respectively, and fixes the c coefficient to the spheric harmonic values. More than 2 mapping factors are required in order to estimate a and b in this method. The iteration limitation and convergence criteria are set to be same with the MFlsmabc and MFlsma methods. The similar unrealistic jumps existing in the MFlsmabc method can also be found in the MFlsmab method when the estimated a_w or b_w coefficients are negative as shown in Fig. 2. Therefore, these situations are also taken as un-convergent.

2.5 MFlsmcom method

We proposed a new method, referred as MFlsmcom, by combining the four mentioned methods according to the convergence performance. The rigorous MFlsmabc method is firstly used to estimate all three coefficients and if the convergence cannot be achieved, the MFlsmab method is then used. If the MFlsmab method is still not convergent, the MFlsma method is applied. It is still possible that the MFlsma method cannot converge the preset convergence criteria, therefore, we also add the MFfast method as the backup of the MFlsma method to ensure the full convergence of the MFlsmcom method in all cases.

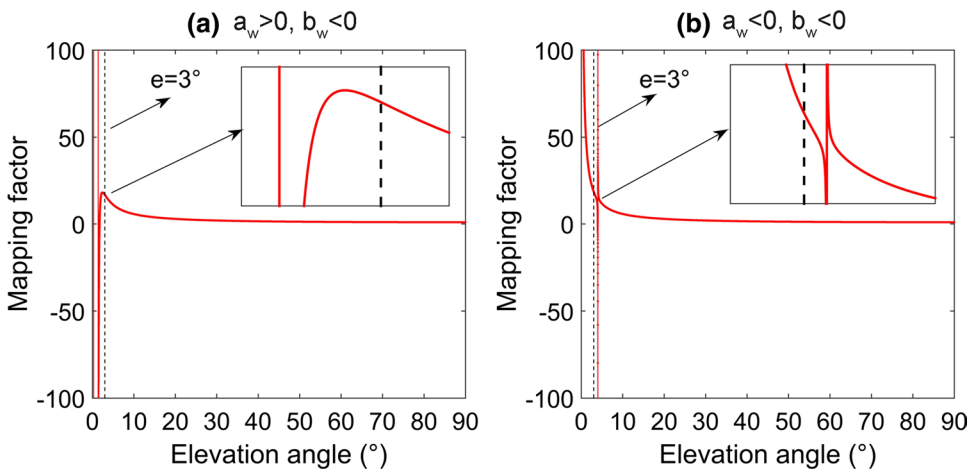

Fig. 2 Fitting curves of wet mapping function coefficients by the MFlsmab method. The a_w, b_w and c_w values are 0.00021392, −0.00208000 and 0.03900876 for the left case **a** and are −0.00004306, -0.00751770 and 0.03900873 for the right case **b**

3 Modeling performance comparisons of different methods

3.1 Tropospheric delay retrieval

The fifth-generation European Centre for Medium-Range Weather Forecasts (ECMWF) Re-Analysis (ERA5) (Hersbach et al. 2019) hourly geopotential, specific humidity and temperature data on 37 pressure levels with 0.25°, 0.50° and 1.00° horizontal resolutions were used to retrieve the hourly ZPDs, including zenith hydrostatic delay (ZHD) and zenith wet delay (ZWD) and SPDs, including slant hydrostatic delay (SHD) and slant wet delay (SWD) (Zhou et al. 2020). These delay products are generated at 14 outgoing elevation angles (3°, 4°, 5°, 6°, 7°, 8°, 10°, 12°, 15°, 20°, 30°, 50°, 70° and 80°) and 16 azimuths (0 ~ 337.5° with an interval of 22.5°) (Landskron 2017; Landskron and Böhm 2018b) during 40 days spanning four seasons in 2020 (season 1: JAN 11 to 20, season 2: APR 11 to 20, season 3: JUL 11 to 20, season 4: OCT 11 to 20) at 905 stations as shown in Fig. 3, including 549 International GNSS Service (IGS) stations and 356 national stations in China. The modified RADIATE software (Hofmeister 2016; Hofmeister and Böhm 2017; Zhou et al. 2020) with two-dimensional (2D) piecewise-linear (2D-PWL) ray-tracing method (Hobiger et al. 2008; Hofmeister and Böhm 2017) is applied to estimate the tropospheric delays. All the calculations are conducted on a supercomputer at Wuhan University.

3.2 Tropospheric mapping function modeling

The 40-day delay products from the 0.25°, 0.50° and 1.00° ERA5 at 3°, 5°, 7°, 10°, 15°, 30° and 70° outgoing elevation angles are used to calculate the mapping factors by dividing the average SPD at 16 azimuths by the ZPDs (Landskron 2017; Landskron and Böhm 2018b). The five methods as described in Sect. 2 were then used to model the mapping factors at all selected 905 stations, deriving five hourly mapping functions. In the modeling, the mapping factors at the seven outgoing elevation angles are taken as inputs for the MFlsmabc, MFlsma, MFlsmab and MFlsmcom methods and the mapping factor at 3° outgoing elevation angle is for the MFfast method (Landskron 2017; Landskron and Böhm 2018b).

3.3 Modeling cost time and convergence ratio

The modeling cost time for the 40-day period by the MFfast method and the four least-squares methods is 26 and 31 min, respectively, which is fast enough for the operational modeling. The convergence ratio is defined as the percent of the epochs reaching convergence in the total 964 epochs (hours in the 40-day period). The average convergence ratios of the 905 stations for the MFlsmabc and MFlsmab methods from 0.25°, 0.50° and 1.00° ERA5 were computed and are shown in Table 1. We can find that the convergent ratios increase with the decrease of the ERA5 horizontal resolution. However, even for 1.00° horizontal resolution, which was commonly used in previous studies, e.g., VMF3, the convergent ratio by using the MFlsmabc method cannot reach 100% for both the hydrostatic and wet components. On the other hand, the MFlsmab method can significantly improve the convergent ratio, for example, from 41.6% to 94.4% (0.25°), 44.6% to 96.8% (0.50°) and 57.7% to 98.1% (1.00°) for the wet component and from incomplete convergence to 100% convergence for the hydrostatic component compared to the MFlsmabc method. The hydrostatic and wet ratios for other three methods are all 100%.

The distribution of the convergence ratios at all modeling stations by using the MFlsmabc and MFlsmab methods from 0.25° ERA5 is compared in Fig. 4a and

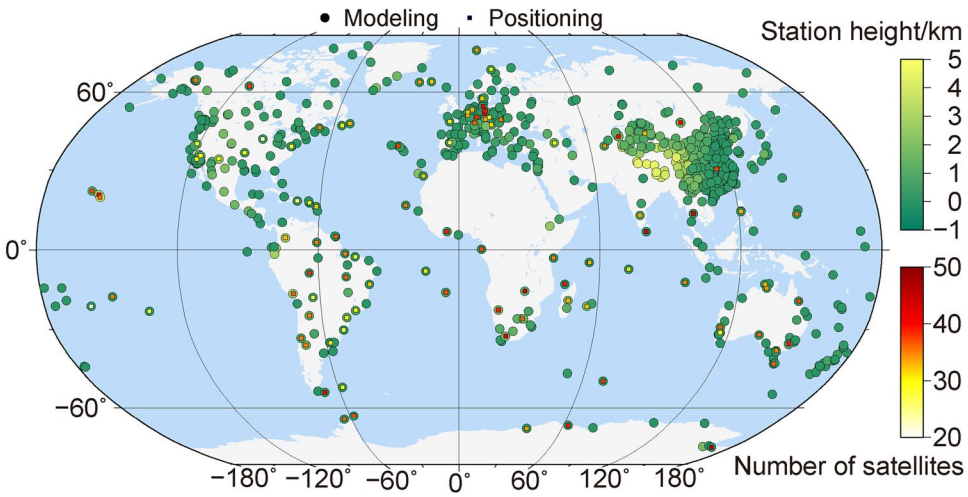

Fig. 3 Distribution of tropospheric modeling stations (circles) and positioning validating stations (squares) and the fill colors of the circles and the squares represent station heights and numbers of average observed GNSS (GPS + GLONASS + GALILEO + BDS3) satellites, respectively

Table 1 Convergence ratios (%) for the MFlsmabc and MFlsmab methods

Methods	Components	0.25°			0.50°			1.00°		
		Min	Max	Mean	Min	Max	Mean	Min	Max	Mean
MFlsmabc	Hydrostatic	36.7	100.0	99.9	97.4	100.0	100.0	99.7	100.0	100.0
MFlsmab		100.0	100.0	100.0	100.0	100.0	100.0	100.0	100.0	100.0
MFlsmabc	Wet	1.5	95.1	41.6	6.5	95.7	44.6	13.3	98.5	57.7
MFlsmab		45.1	100.0	94.4	47.7	100.0	96.8	65.4	100.0	98.1

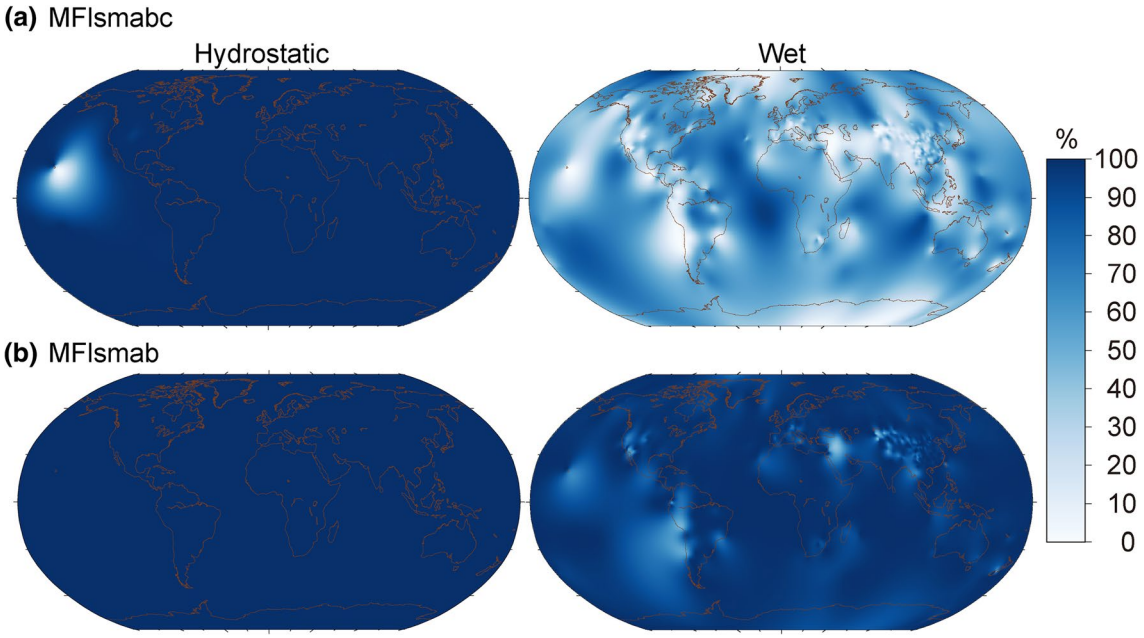

Fig. 4 Distribution of average modeling convergence ratio by using the MFlsmabc **a** and MFlsmab **b** methods for hydrostatic (left) and wet (right) components

b, respectively. We can find that the stations with lower hydrostatic convergence ratio by MFlsmabc method are mainly in the North Pacific and North America (left column of Fig. 4a). The MKEA station (in Mauna Kea, Hawaii, USA, North Pacific) with ellipsoidal height of 3755 m has the lowest hydrostatic convergence ratio, with values of 36.7%, 97.4% and 100% for 0.25°, 0.50° and 1.00° ERA5, respectively, which should be related to the surrounding complex topography (Fig. 5). The stations with lower wet convergence ratio by MFlsmabc method are globally distributed, and the proportion of stations with wet convergence ratio smaller than 50% and 10% is 61.3% and 4.5%, respectively (right column of Fig. 4a). The convergence performance for the MFlsmab method is much better, especially for the wet component, and the proportion of stations with average wet convergence ratio lower than 90% and 50% is only 15.7% and 0.3%, respectively (Fig. 4b).

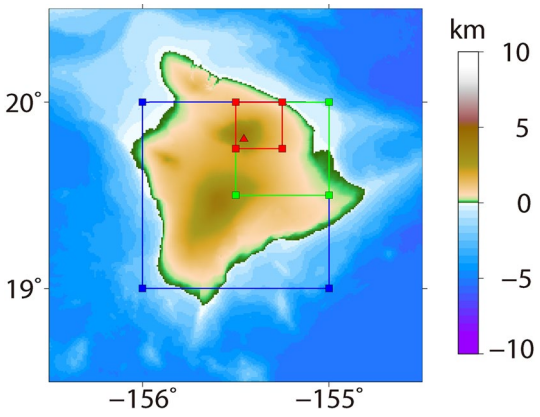

Fig. 5 Topography for 0.25° (red squares), 0.50° (green squares) and 1.00° (blue squares) ERA5 around station MKEA. The station location is represented by the red triangle

3.4 Modeling residual error

The un-convergent epochs are excluded in the modeling residual error evaluation. The modeling residual errors of the five methods are evaluated by comparing with ray-traced SPD at 3°, 5°, 7°, 10°, 15°, 30° and 70° elevation angles (involved in the mapping function modeling), by using the mean absolute error (MAE) as the precision index (Urquhart et al. 2014; Landskron 2017; Landskron and Böhm 2018b). The 40-day average modeling residual MAEs by the five methods from 0.25° ERA5 were calculated at the convergent epochs of the MFlsmabc method for evaluating the accuracy of the five methods, and the statistical results are summarized in Table 2. The MAEs at 3° elevation angle for the MFfast method are 0.0 mm, due to the fact that the MFfast method only takes the mapping factor at 3° elevation angle as modeling inputs. The MAEs of the MFlsmcom method are same as the MFlsmabc method, and the reason is that the MFlsmcom method simply inherits the MFlsmabc method at the epochs when the MFlsmabc method can reach convergence. The hydrostatic and wet MAEs of the MFlsmabc method for all elevation angles are smaller than 0.3 and 0.1 mm, respectively, which are better than the MFlsmab method (0.9 and 0.2 mm) and much better than the MFlsma (1.9 and 1.9 mm) and MFfast (2.2 and 2.1 mm) methods.

The modeling residual MAEs for the five methods at their own convergent epochs are also summarized in Table 3. The maximal hydrostatic and wet MAEs among all elevation angles for the MFlsmabc method are 0.3 and 0.1 mm, which are smaller than the MFlsmab method (0.9 and 0.4 mm) and much smaller than the MFlsma (1.9 and 2.8 mm) and MFfast (2.2 and 3.1 mm) methods. Regarding the MFlsmcom method, the maximal hydrostatic and wet MAEs are 0.3 and 0.8 mm that are much better than the MFlsma and MFfast methods and similar to the MFlsmabc method for the hydrostatic components.

As shown in Table 3, the modeling residual MAEs at 5° elevation angle are generally the largest; therefore, we further presented the MAE distribution at 5° elevation angle for the five methods in Fig. 6. The MAEs of the MFlsmabc method are very small in the globe, with the hydrostatic and wet MAEs for all station smaller than 0.3 and 0.1 mm (Fig. 6a). The MAE distribution of the MFlsmab method is slightly worse than the MFlsmabc method, with maximal MAEs of 2.1 and 1.7 mm for the hydrostatic and wet components, respectively (Fig. 6b). The MAE distribution of the MFlsma and MFfast methods is similar (slightly different in MAE values) and obviously worse than the MFlsmabc and MFlsmab methods (Fig. 6c and d). The larger hydrostatic MAEs of the MFfast method are globally distributed,

Table 2 Modeling residual MAEs (mm) for the five methods at the convergent epochs of the MFlsmabc method

Methods	Components	e = 3°	e = 5°	e = 7°	e = 10°	e = 15°	e = 30°	e = 70°
MFlsmabc	Hydrostatic	0.01	0.09	0.29	0.20	0.29	0.08	0.00
MFlsmab		0.08	0.70	0.86	0.50	0.21	0.05	0.00
MFlsma		0.90	1.92	1.64	0.89	0.35	0.07	0.00
MFfast		0.00	2.23	1.75	0.93	0.36	0.07	0.00
MFlsmcom		0.01	0.09	0.29	0.20	0.29	0.08	0.00
MFlsmabc	Wet	0.00	0.02	0.08	0.06	0.10	0.04	0.00
MFlsmab		0.01	0.12	0.14	0.16	0.12	0.04	0.00
MFlsma		0.72	1.87	1.22	0.56	0.21	0.04	0.00
MFfast		0.00	2.08	1.30	0.59	0.22	0.04	0.00
MFlsmcom		0.00	0.02	0.08	0.06	0.10	0.04	0.00

Table 3 Modeling residual MAEs (mm) for the five methods at their own convergent epochs

Methods	Components	e = 3°	e = 5°	e = 7°	e = 10°	e = 15°	e = 30°	e = 70°
MFlsmabc	Hydrostatic	0.01	0.09	0.29	0.20	0.29	0.08	0.00
MFlsmab		0.08	0.70	0.86	0.50	0.21	0.05	0.00
MFlsma		0.90	1.92	1.64	0.89	0.35	0.07	0.00
MFfast		0.00	2.23	1.76	0.93	0.36	0.07	0.00
MFlsmcom		0.01	0.10	0.29	0.20	0.29	0.08	0.00
MFlsmabc	Wet	0.00	0.02	0.08	0.06	0.10	0.04	0.00
MFlsmab		0.03	0.32	0.35	0.44	0.27	0.06	0.00
MFlsma		1.08	2.75	1.99	1.07	0.45	0.08	0.00
MFfast		0.00	3.06	2.12	1.12	0.46	0.08	0.00
MFlsmcom		0.21	0.75	0.64	0.54	0.31	0.07	0.00

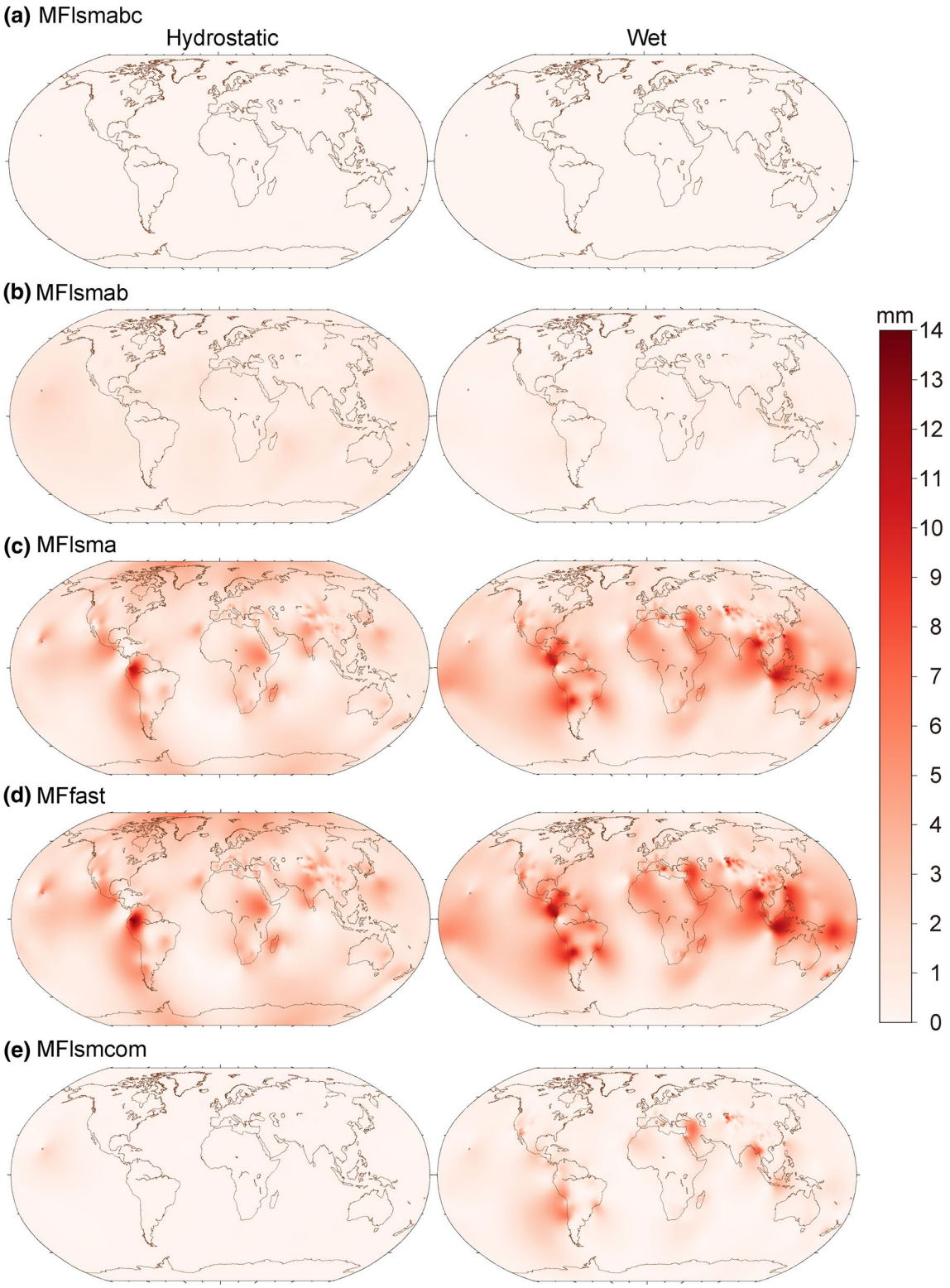

Fig. 6 Distribution of modeling residual MAEs at 5° elevation angle for the hydrostatic (left) and wet (right) components by using the MFlsmabc **a**, MFlsmab **b**, MFlsma **c**, MFfast **d** and MFlsmcom **e** methods

especially for stations in the Northwest South America, with MAE reaching about 9.4 mm (left column of Fig. 6d). The proportion of the hydrostatic MAEs larger than 5 mm is 3.5%. The MAEs of the MFfast method in the wet component are even larger than the hydrostatic component and are generally correlated with the station latitudes. The low-latitude regions, especially near the equator, generally with more abundant and more variable tropospheric water vapor (Nikolaidou et al. 2018), show larger MAEs, with maximal MAE of 13.1 mm (right column of Fig. 6d). The proportion of the wet MAEs larger than 10 and 5 mm is 0.8% and 12.8%, respectively. The MAEs of the MFlsmcom method for all stations are smaller than 1.4 and 7.7 mm that are also much better than the MFlsma and MFfast methods (Fig. 6e).

4 Mapping function validations by ray-traced SPD

The incompletely convergent MFlsmabc and MFlsmab methods cannot be used in operational mapping function modeling and therefore were excluded in the following mapping function validations and multi-GNSS PPP evaluations. The mapping functions by the fully convergent MFlsma, MFfast and MFlsmcom methods from 0.25° ERA5 will be validated in this section. The ray-traced SPDs at 4°, 6°, 8°, 12°, 20°, 50° and 80° elevation angles are not used in the mapping function modeling and therefore can be used as independent data to evaluate the accuracy of the mapping functions from the three methods. The 40-day SPD time series at all selected 905 stations were recovered at 4°, 6°, 8°, 12°, 20°, 50° and 80° elevation angles by using the three mapping functions and compared with the ray-traced SPDs, yielding the 40-day average MAEs as shown in Table 4. The validating MAEs of the three methods have significant differences at the elevation angles lower than 20° and the MAEs of the MFlsmcom method (1.6 and 1.3 mm) are obviously smaller than MAEs of the MFlsma (3.4 and 2.4 mm) and MFfast (3.6 and 3.0 mm) methods, indicating the significant improvement of the new proposed MFlsmcom method in tropospheric mapping function modeling.

The MAEs at 4° elevation angle are generally largest in the seven elevation angles, and the MAE distribution at 4° elevation angle for the three methods is therefore presented in Fig. 7. The MFlsma and MFfast methods show slightly different MAE values but similar MAE distribution (Fig. 7a and b). The larger hydrostatic MAEs for the MFfast method are globally distributed, and the stations in the Northwest South America have the much larger hydrostatic MAEs, with maximal MAE of 11.2 mm (left column of Fig. 7b). The proportion of the hydrostatic MAEs larger than 10 and 5 mm is 0.7% and 14.7%. The wet MAEs for the MFfast method show dependences on the station latitude where low-latitude stations have obviously larger wet MAEs, with maximal MAE of 11.8 mm (right column of Fig. 7b). The proportion of the wet MAEs larger than 10 and 5 mm is 0.7% and 10.7%. The MAE for the MFlsmcom method is obviously smaller than the MFlsma and MFfast methods. The hydrostatic MAEs for the MFlsmcom method are smaller than 3 mm for all stations except for the MKEA station in the North Pacific, with maximal MAE of 3.6 mm (left column of Fig. 7c). The proportion of the hydrostatic MAEs larger than 2 mm is 5.9%. The wet MAEs of the MFlsmcom method also show latitude dependence but have much smaller values compared with the MFlsma and MFfast methods, with maximal MAE of 7.5 mm (right column of Fig. 7c). The proportion of the wet MAEs larger than 5 and 2 mm is 1.2% and 14.0%.

5 Mapping function evaluations in multi-GNSS PPP

5.1 PPP data processing strategy

The GNSS PPP performance by using the mapping functions from the MFlsma, MFfast and MFlsmcom methods and 0.25° ERA5 will be investigated in this section. The globally distributed 107 multi-GNSS (GPS + GLONASS + GALILEO + BDS3) stations as shown in Fig. 3 from IGS Multi-GNSS Experiment (MGEX) campaign (Montenbruck et al. 2017) are selected for the multi-GNSS PPP validations. We used the Positioning And Navigation Data Analyst (PANDA) software (Shi et al. 2008) to process the 300 s GNSS data spanning four seasons in 2020 (season 1: JAN 11 to 20, season 2: APR 11 to 20, season 3: JUL 11 to 20, season 4: OCT

Table 4 MAEs (mm) for the MFlsma, MFfast and MFlsmcom methods

Methods	Components	e = 4°	e = 6°	e = 8°	e = 12°	e = 20°	e = 50°	e = 80°
MFlsma	Hydrostatic	3.37	1.80	1.38	0.60	0.19	0.04	0.03
MFfast		3.56	1.99	1.46	0.62	0.20	0.04	0.03
MFlsmcom		1.63	0.38	0.19	0.31	0.20	0.04	0.03
MFlsma	Wet	2.44	2.45	1.64	0.76	0.25	0.04	0.03
MFfast		2.97	2.64	1.72	0.78	0.25	0.04	0.03
MFlsmcom		1.31	0.70	0.71	0.48	0.20	0.04	0.03

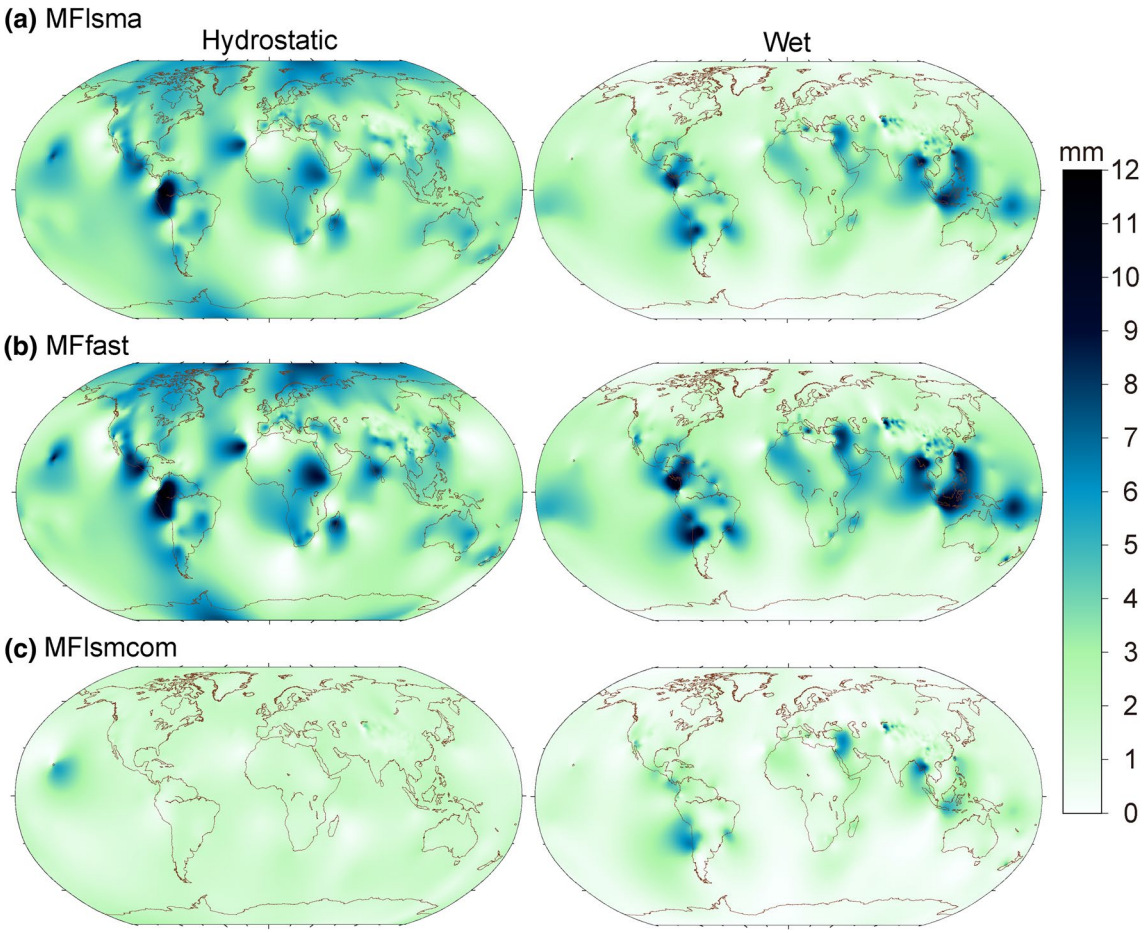

Fig. 7 Distribution of validating MAEs at 4° elevation angle for the hydrostatic (left) and wet (right) components by using the MFlsma **a**, MFfast **b** and MFlsmcom **c** methods

11 to 20). The GFZ GBM GNSS satellite orbit products were fixed, and the satellite clock corrections were estimated every 300 s with the modeled mapping functions used to exclude the influences of inconsistency of mapping functions in GBM clock products on the later PPP. Three PPP schemes were carried out with mapping functions from the three methods used, and the data processing strategies are listed in Table 5. In the data processing, the time interpolations are necessary for the application of the mapping functions. Separately interpolating the a, b and c coefficients may have the risks of ignoring the inherent high correlation among coefficients which may cause incorrect calculation of the mapping factors (Böhm 2004). We therefore alternatively interpolated the mapping factors at specific observed elevation angle to the GNSS data epoch time.

5.2 PPP coordinate repeatability

The station coordinate repeatability of the three PPP schemes will be compared in this section. The 10-day daily station coordinate time series from the multi-GNSS PPP were used to calculate the coordinate repeatability at each season. The atmospheric pressure loading (APL) has non-negligible influences on the coordinate repeatability of space geodetic techniques (Steigenberger et al. 2009) and therefore needs to be corrected from the daily PPP coordinate time series by using APL products from Technische Universitat Wien (Tregoning and Dam 2005; Wijaya et al. 2013), yielding the coordinate repeatability without and with APL correction for the PPP schemes by using the three mapping functions in Table 6.

The coordinate repeatability shows the seasonal variations with the worst and the best repeatability for the season 1 (JAN) and season 4 (OCT), respectively. The APL correction can improve the vertical (U) coordinate repeatability, while slightly contaminate the north (N) and east (E) coordinate repeatability. The coordinate repeatability by using the mapping functions from the three methods is almost identical in the horizontal components and slightly different in the vertical components, and the reason is that the impacts

Table 5 Data processing strategies for multi-GNSS PPP

Observation	
Sampling interval	300 s
Frequency combination	Ionosphere-free combination
Elevation cutoff angle	3°
Elevation weighting strategy	$\begin{cases} p = 4sin^2e, (e \le 30°) \\ p = 1, (e > 30°) \end{cases}$
Error correction	
Phase center variations	igs14.atx
Ocean tide loading	FES2014b
A priori tropospheric delay	Scheme 1: MFlsma + ZPD Scheme 2: MFfast + ZPD Scheme 3: MFlsmcom + ZPD
Parameter estimation	
Satellite orbits	Fixed from GBM 5 min products
Satellite clock corrections	Fixed from estimated 5 min products
Mapping function	Scheme 1: Wet MFlsma Scheme 2: Wet MFfast Scheme 2: Wet MFlsmcom
ZWD stochastic model	Piece-wise constant (1 h), random walk between segments ($15\,mm/\sqrt{h}$)
Gradient mapping function	$mf_w \bullet \cot(e)$(Bar-Sever et al. 1998)
Gradient stochastic model	Piece-wise constant (1 h), random walk between segments ($10\,mm/\sqrt{h}$)
Station coordinates	Daily constant
Receiver clock corrections	White noise
Ambiguities	Fixed

of different mapping functions on the coordinate repeatability are greatly blocked by the numerical weather model (ERA5) and ray-tracing algorithm (2D-PWL) errors in the tropospheric delay retrieval (Nafisi et al. 2011), the time interpolation errors in the application of the mapping functions, the elevation-dependent weighting strategy in the data processing and the unmodeled errors, such as solid earth tide (Watson et al. 2006), in the GNSS coordinate time series.

The PPP solution with the mapping function from the MFlsmcom method has a little worse vertical coordinate repeatability compared with the solution schemes by using the mapping functions from the MFlsma and MFfast methods. One of the possible reasons may be that most current correction models in the GNSS data processing are more consistent with the mapping function from the MFlsma and MFfast methods, e.g., VMF1, resulting in marginal better coordinate repeatability in MFlsma and MFfast solutions. In addition, there are still 45 stations in 107 stations with better coordinate repeatability for the MFlsmcom method than for the MFfast method, indicating that the statistical results may be also affected by the samples. Furthermore, one should realize the fact that the coordinate repeatability is only related to the standard deviation of the coordinate time series. The potential improvement in the systematic bias of estimated coordinates requires further investigations in the future when the absolute reference is available.

5.3 Differences of PPP estimated coordinate and ZTD

The station coordinate repeatability cannot reflect the potential coordinate biases, and we therefore directly compared the estimated coordinates and ZTD from three PPP solutions. The slant total delays (STDs) at 5° elevation angle calculated from the ray-traced ZPD and three mapping functions were also compared in this section, with the

Table 6 PPP coordinate repeatability (mm) by using the mapping functions from the three methods

Seasons	Methods	Without APL correction			With APL correction		
		N	E	U	N	E	U
Season 1	MFlsma	1.14	1.17	4.09	1.26	1.19	3.56
	MFfast	1.13	1.17	4.08	1.26	1.19	3.55
	MFlsmcom	1.13	1.17	4.12	1.25	1.19	3.59
Season 2	MFlsma	0.95	0.94	3.56	0.98	0.97	3.28
	MFfast	0.95	0.94	3.56	0.98	0.97	3.28
	MFlsmcom	0.95	0.94	3.58	0.98	0.97	3.31
Season 3	MFlsma	1.03	1.12	3.48	1.13	1.11	3.30
	MFfast	1.03	1.12	3.47	1.13	1.12	3.29
	MFlsmcom	1.03	1.12	3.53	1.14	1.12	3.35
Season 4	MFlsma	0.93	0.88	3.43	0.97	0.93	3.13
	MFfast	0.93	0.88	3.43	0.96	0.93	3.13
	MFlsmcom	0.94	0.87	3.44	0.97	0.93	3.16
Mean	MFlsma	1.01	1.02	3.64	1.08	1.05	3.32
	MFfast	1.01	1.02	3.64	1.08	1.05	3.32
	MFlsmcom	1.01	1.02	3.67	1.09	1.05	3.35

averaged bias, root mean square (RMS) and standard deviations (STDEV) summarized in Table 7. The impacts of the mapping function on the horizontal coordinate differences are negligible and therefore not included in Table 7. The MFlsma and MFfast methods have almost equivalent results; therefore, for simplification, we only present comparisons of MFfast and MFlsmcom methods in this section.

The STD, vertical coordinate and ZTD difference RMSs also show seasonal variations. The largest RMSs for the three components are in season 3 (JUL), season 1 (JAN) and season 1 (JAN), respectively, with values of 5.37, 0.67 and 0.42 mm. The mapping functions mainly influence the vertical coordinate estimation, with seasonal average RMS and STDEV of 0.65 and 0.42 mm, which are approximately 1.6 and 1.4 times of the mean ZTD RMS and STDEV, respectively. The mean biases of the vertical coordinate and ZTD differences are -0.10 and 0.14 mm, indicating the potential systematic deviations in PPP results between using mapping functions modeled with the MFfast and MFlsmcom methods.

Season 3 shows the largest STD difference RMS and, therefore, we further showed the difference bias and RMS distribution of the STD (5°), station height (U) and ZTD for season 3 in Fig. 8. The modeled STD (5°) biases at some stations are almost equal to their RMSs (Fig. 8a), such as BOGT station (in Bogota, Colombia, North South America) with bias and RMS of 11.25 and 11.60 mm, illustrating the exist of systemic biases of the modeled STDs between the MFfast and MFlsmcom methods. The proportions of absolute STD biases larger than 10 and 5 mm are 0.9% and 12.1%. Interestingly, the distribution of the station height bias is similar to the STD (5°) bias (Fig. 8a and b), indicating that the station height biases are affected by the modeled STD biases. The error conversion factors between the STD (5°) and station height for the bias and RMS are 0.17 and 0.12, respectively, which are smaller than the published 'rule-of-thumb' values of 0.22 or 1/5 (MacMillan and Ma 1994; Boehm 2004), mainly due to the use of cutoff elevation angle of 3° and elevation-dependent weighting strategy in our case (MacMillan and Ma 1994; Kouba 2009). In addition, the rule-of-thumb is also influenced by the actual distribution of the observation elevation angles (Böhm et al. 2006). The proportions of absolute station height biases larger than 2 and 1 mm are 0.9% and 4.7%. The ZTD biases are opposite in sign to station height biases and, if reverse the signs of the ZTD biases, we can see the almost identical distribution between ZTD biases and the station height biases (Fig. 8b and c), illustrating the strong correlations between the station height and ZTD. The proportion between height and ZTD is 1.80 and 1.56 for the bias and RMS, respectively, which are close to the value of about 2.0 reported by Tregoning and Herring (2006). The proportions of absolute ZTD biases larger than 1 and 0.5 mm are 0.9% and 14.0%. The MFlsmcom method shows its considerable impacts on the station height and ZTD estimation at some stations.

6 Conclusions

In this paper, on the basis of the existing MFlsmabc, MFlsma and MFfast methods, we presented the MFlsmab method and the new MFlsmcom method for better handling of the coefficients in mapping function modeling and comprehensively evaluated the modeling cost time, convergence ratio and modeling error of the five methods. We found that the modeling cost time by using different methods is almost

Table 7 Modeled STD as well as PPP estimated vertical coordinate and ZTD differences (mm) between the mapping functions from the three methods

Seasons	Components	MFlsmcom minus MFlsma			MFlsmcom minus MFfast		
		Bias	RMS	STDEV	Bias	RMS	STDEV
Season 1	STD	0.51	4.40	3.72	0.53	4.99	4.19
	U	−0.15	0.63	0.42	−0.15	0.67	0.44
	ZTD	0.17	0.41	0.29	0.17	0.42	0.29
Season 2	STD	0.99	4.38	3.54	1.11	4.96	3.97
	U	−0.09	0.60	0.38	−0.07	0.64	0.41
	ZTD	0.13	0.38	0.27	0.12	0.40	0.28
Season 3	STD	0.77	4.75	3.86	0.88	5.37	4.33
	U	−0.13	0.60	0.38	−0.12	0.64	0.40
	ZTD	0.15	0.39	0.28	0.14	0.41	0.30
Season 4	STD	0.96	4.19	3.51	1.08	4.73	3.95
	U	−0.08	0.60	0.41	−0.07	0.64	0.44
	ZTD	0.13	0.37	0.28	0.13	0.39	0.29
Mean	STD	0.80	4.43	3.66	0.90	5.01	4.11
	U	−0.11	0.61	0.40	−0.10	0.65	0.42
	ZTD	0.15	0.39	0.28	0.14	0.40	0.29

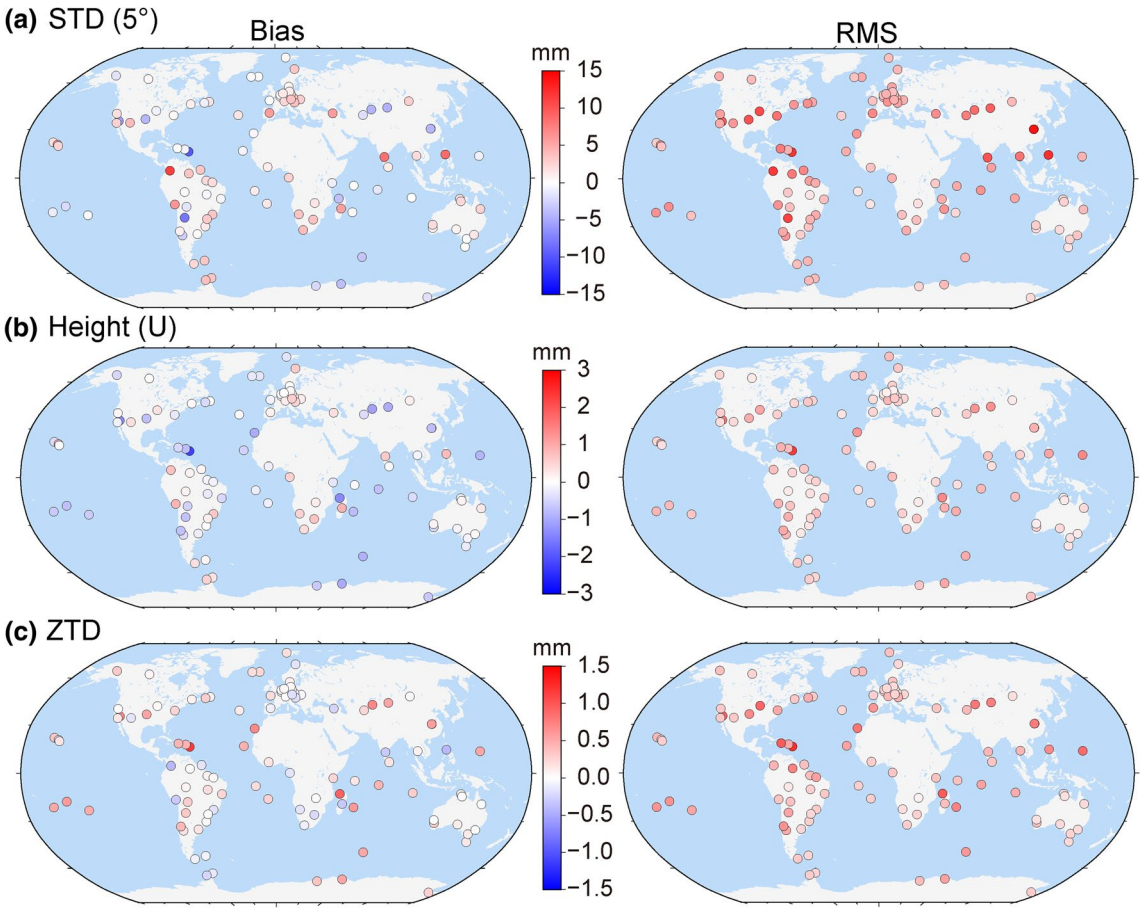

Fig. 8 Difference bias and RMS distribution between the mapping functions from the MFfast and MFlsmcom methods for modeled STD (5°) **a** and PPP estimated station height (U) **b** and ZTD **c**

identical and fast enough for operational modeling. The rigorous MFlsmabc method is characterized by high accuracy (with hydrostatic and wet modeling residual MAEs of 0.3 and 0.1 mm) but non-ideal convergence for wet mapping function modeling (with wet convergence ratio of 41.6%). The MFlsmab method can significantly improve the wet convergence ratios (from 41.6% to 94.4%) with negligible loss of accuracy (with hydrostatic and wet MAEs of 0.9 and 0.4 mm) compared with the MFlsmabc method. Both MFlsma and MFfast methods are 100% convergence, while their modeling accuracy is significant degraded, with hydrostatic and wet MAEs of 1.9 and 2.8 mm for the MFlsma method and of 2.2 and 3.1 mm for the MFfast method. The MFlsmcom method inherits the high accuracy of the MFlsmabc and MFlsmab methods and the high convergence ratio of the MFlsma method and therefore, with hydrostatic and wet MAEs of 0.3 and 0.8 mm and 100% convergence, performs much better than the MFlsma and MFfast methods.

In addition, the mapping functions from the fully convergent MFlsma, MFfast and MFlsmcom methods were validated by the ray-traced SPDs at 4°, 6°, 8°, 12°, 20°, 50° and 80° elevation angles (not involved in the modeling). The mapping function from the MFlsmcom method with hydrostatic and wet validating MAEs of 1.6 and 1.3 mm is obviously better than the mapping functions from the MFlsma (3.4 and 2.4 mm) and MFfast (3.6 and 3.0 mm) methods, indicating the significant improvement of the new proposed MFlsmcom method in tropospheric mapping function modeling. The modeled STD and multi-GNSS PPP estimated coordinate and ZTD from the MFlsma, MFfast and MFlsmcom methods were also compared. The MFlsma and MFfast methods show almost identical modeled STD and PPP performances, while the STD and PPP results of the MFfast and MFlsmcom methods differ a lot. We found the significant systemic biases of the modeled STDs (with maximal bias of 11.2 mm) between the MFfast and MFlsmcom methods that induce the remarkable station height and ZTD biases (with maximal biases of 2.2 and 1.1 mm), indicating the effectiveness of the new MFlsmcom method in multi-GNSS PPP analyses.

Acknowledgements This work was supported by the National Natural Science Foundation of China (41774036; 41804023; 41961144015) and the Fundamental Research Funds for the Central Universities (2042020kf0020). Authors would like to thank Copernicus Climate Data Store, IGS CDDIS and GFZ for providing the research datasets and products and acknowledge Technische Universität Wien for developing the ray-tracing package RADIATE and releasing APL products. The numerical calculations in this paper have been done on the supercomputing system in the Supercomputing Center of Wuhan University.

Author contributions YDL and WXZ initiated the study. YZZ, WXZ and YDL proposed the conceptual ideas and designed and performed the experiments with the help and support from JNB and ZYZ. YZZ, WXZ and YDL were involved in the manuscript writing. All authors read and approved the final manuscript.

Declarations

Data Availability ERA5 was downloaded from Copernicus Climate Data Store (https://cds.climate.copernicus.eu/). IGS MGEX RINEX data and GFZ GBM satellite orbit product are available through IGS CDDIS FTP (ftp://gdc.cddis.eosdis.nasa.gov/) and GFZ FTP (ftp://ftp.gfz-potsdam.de/). APL products were downloaded from Technische Universität Wien (http://vmf.geo.tuwien.ac.at/).

References

Bar-Sever YE, Kroger PM, Borjesson JA (1998) Estimating horizontal gradients of tropospheric path delay with a single GPS receiver. J Geophys Res Solid Earth 103(B3):5019–5035. https://doi.org/10.1029/97JB03534

Böhm J (2004) Troposphärische Laufzeitverzögerungen in der VLBI. Doctoral Dissertation, Institut für Geodäsie und Geophysik, TU Wien, Supervisor: Schuh H. https://publik.tuwien.ac.at/files/PubDat_119666.pdf

Böhm J, Schuh H (2004) Vienna mapping functions in VLBI analyses. Geophys Res Lett 31(1). https://doi.org/10.1029/2003GL018984

Böhm J, Schuh H (2007) Troposphere gradients from the ECMWF in VLBI analysis. J Geod 81(6):403–408. https://doi.org/10.1007/s00190-007-0144-2

Böhm J, Werl B, Schuh H (2006) Troposphere mapping functions for GPS and very long baseline interferometry from European Centre for Medium-Range Weather Forecasts operational analysis data. J Geophys Res Solid Earth 111(B2). https://doi.org/10.1029/2005JB003629

Herring TA (1992) Modeling atmospheric delays in the analysis of space geodetic data. In: DeMunck JC, Spoelstra TAT (eds) Publications on geodesy, vol 36. Proceedings of refraction of transatmospheric signals in geodesy. The Hague, Netherlands, Netherlands Geodetic Commission Publications in Geodesy, pp 157–164

Hersbach H, Bell B, Berrisford P, Horányi A, Sabater JM, Nicolas J, Dee D (2019) Global reanalysis: goodbye ERA-Interim, hello ERA5. ECMWF Newsletters, 159, 17–24. https://www.ecmwf.int/node/19027

Hobiger T, Ichikawa R, Koyama Y, Kondo T (2008) Fast and accurate ray-tracing algorithms for real-time space geodetic applications using numerical weather models. J Geophys Res Atmos 113(D20). https://doi.org/10.1029/2008JD010503

Hofmeister A (2016) Determination of path delays in the atmosphere for geodetic VLBI by means of ray-tracing. Doctoral Dissertation, Department of Geodesy and Geoinformation, TU Wien, Supervisor: Böhm J. http://resolver.obvsg.at/urn:nbn:at:at-ubtuw:1-3444

Hofmeister A, Böhm J (2017) Application of ray-traced tropospheric slant delays to geodetic VLBI analysis. J Geod 91(8):945–964. https://doi.org/10.1007/s00190-017-1000-7

Kouba J (2009) Testing of global pressure/temperature (GPT) model and global mapping function (GMF) in GPS analyses. J Geod 83(3–4):199–208. https://doi.org/10.1007/s00190-008-0229-6

Landskron D (2017) Modeling tropospheric delays for space geodetic techniques. Doctoral Dissertation, Department of Geodesy and Geoinformation, TU Wien, Supervisor: Böhm J. http://repositum.tuwien.ac.at/obvutwhs/content/titleinfo/2099559

Landskron D, Böhm J (2018a) Refined discrete and empirical horizontal gradients in VLBI analysis. J Geod 92(12):1387–1399. https://doi.org/10.1007/s00190-018-1127-1

Landskron D, Böhm J (2018b) VMF3/GPT3: refined discrete and empirical troposphere mapping functions. J Geod 92(4):349–360. https://doi.org/10.1007/s00190-017-1066-2

Liu J, Gao K, Guo W, Cui J, Guo C (2020) Role, path and vision of "5G + BDS/GNSS." Satell Navig 1(1):23. https://doi.org/10.1186/s43020-020-00024-w

Lu C, Zus F, Heinkelmann R, Dick G, Ge M, Wickert J, Schuh H (2016) Tropospheric delay parameters from numerical weather models for multi-GNSS precise positioning. Atmos Meas Tech 9:5965–5973. https://doi.org/10.5194/amt-9-5965-2016

MacMillan DS, Ma C (1994) Evaluation of very long baseline interferometry atmospheric modeling improvements. J Geophys Res Solid Earth 99(B1):637–651. https://doi.org/10.1029/93JB02162

Marini JW (1972) Correction of satellite tracking data for an arbitrary tropospheric profile. Radio Sci 7(2):223–231. https://doi.org/10.1029/RS007i002p00223

Montenbruck O, Steigenberger P, Prange L, Deng Z, Zhao Q, Perosanz F, Schaer S (2017) The Multi-GNSS Experiment (MGEX) of the International GNSS Service (IGS)–achievements, prospects and challenges. Adv Space Res 59(7):1671–1697. https://doi.org/10.1016/j.asr.2017.01.011

Nafisi V, Urquhart L, Santos MC, Nievinski FG, Bohm J, Wijaya DD, Zus F (2011) Comparison of ray-tracing packages for troposphere delays. IEEE Trans Geosci Remote Sens 50(2):469–481. https://doi.org/10.1109/TGRS.2011.2160952

Niell AE (1996) Global mapping functions for the atmosphere delay at radio wavelengths. J Geophys Res Solid Earth 101(B2):3227–3246. https://doi.org/10.1029/95JB03048

Nikolaidou T, Balidakis K, Nievinski FG, Santos MC, Schuh H (2018) Impact of different NWM-derived mapping functions on VLBI and GPS analysis. Earth Planets Space 70(1):1–16. https://doi.org/10.1186/s40623-018-0865-x

Santos MC, McAdam MP, Böhm J (2012) Implementation Status of the UNB-VMF1. Geophysical Research Abstracts, European Geosciences Union General Assembly (EGU 2012), 22–27, Vienna, Vol.14, EGU2012–13759. http://unb-vmf1.gge.unb.ca/publications/EGU2012-poster-UNB-VMF1.pdf

Shi C, Zhao Q, Geng J, Lou Y, Ge M, Liu J (2008) Recent development of PANDA software in GNSS data processing. In: International Conference on Earth Observation Data Processing and Analysis (ICEODPA) (Vol. 7285, p. 72851S). International Society for Optics and Photonics. https://doi.org/10.1117/12.816261

Steigenberger P, Boehm J, Tesmer V (2009) Comparison of GMF/GPT with VMF1/ECMWF and implications for atmospheric loading. J Geod 83(10):943–951. https://doi.org/10.1007/s00190-009-0311-8

Tregoning P, Dam TV (2005) Atmospheric pressure loading corrections applied to GPS data at the observation level. Geophys Res Lett 32(22). https://doi.org/10.1029/2005GL024104

Tregoning P, Herring TA (2006) Impact of a priori zenith hydrostatic delay errors on GPS estimates of station heights and zenith total delays. Geophys Res Lett 33(23). https://doi.org/10.1029/2006GL027706

Urquhart L, Nievinski FG, Santos MC (2014) Assessment of troposphere mapping functions using three-dimensional ray-tracing. GPS Solut 18(3):345–354. https://doi.org/10.1007/s10291-013-0334-8

Watson C, Tregoning P, Coleman R (2006) Impact of solid Earth tide models on GPS coordinate and tropospheric time series. Geophys Res Lett 33(8). https://doi.org/10.1029/2005GL025538

Wijaya DD, Böhm J, Karbon M, Kràsnà H, Schuh H (2013) Atmospheric pressure loading. In: Atmospheric effects in space geodesy (pp. 137–157). Springer, Berlin, Heidelberg. https://link.springer.com/book/https://doi.org/10.1007/978-3-642-36932-2

Zhou Y, Lou Y, Zhang W, Kuang C, Liu W, Bai J (2020) Improved performance of ERA5 in global tropospheric delay retrieval. J Geod 94(10):1–14. https://doi.org/10.1007/s00190-020-01422-3

Zumberge JF, Heflin MB, Jefferson DC, Watkins MM, Webb FH (1997) Precise point positioning for the efficient and robust analysis of GPS data from large networks. J Geophys Res Solid Earth 102(B3):5005–5017. https://doi.org/10.1029/96JB03860

Zus F, Dick G, Douša J, Wickert J (2015) Systematic errors of mapping functions which are based on the VMF1 concept. GPS Solut 19:277–286. https://doi.org/10.1007/s10291-014-0386-4